IEEE Open Journal of
Industry Applications

Received 20 October 2025; revised 7 January 2026; accepted 8 February 2026. Date of publication 10 February 2026;
date of current version 25 February 2026.

Digital Object Identifier 10.1109/OJIA.2026.3663542

S-Shaped-Based Power Sharing Control of DC-Coupled EV Charging Station

MÁRCIO VON RONDOW CAMPOS [1], LUCAS JONYS RIBEIRO SILVA [1] (Graduate Student Member, IEEE), DENIVER REINKE SCHUTZ [1], THALES AUGUSTO FAGUNDES [1], BRUNO MENEGHEL ZILLI [2], RODOLPHO VILELA ALVES NEVES [3], AND RICARDO QUADROS MACHADO [1] (Senior Member, IEEE)

[1]Sao Carlos School of Engineering, University of Sao Paulo, Sao Carlos, SP 13566-590, Brazil
[2]Federal University of Technology-Paraná, Guarapuava, PR 85053-525, Brazil
[3]Federal University of Viçosa, Viçosa, MG 36570-900, Brazil

CORRESPONDING AUTHOR: MÁRCIO VON RONDOW CAMPOS (e-mail: marciovonrondow@usp.br)

This work was supported in part by the Coordination for the Improvement of Higher Education Personnel (CAPES) under Grant 88887.482911/2020-00 and Grant 88887.182131/2025-00, in part by the National Council for Scientific and Technological Development (CNPq) under Grant 301148/2025-2, and in part by the Sao Paulo Research Foundation (FAPESP) under Grant 2020/05865-3, Grant 2022/00628-9, Grant 2023/06759-0, and Grant 2024/00607-7.

ABSTRACT This work proposes an S-shaped power-sharing control (S-PSC) for enhancing scalability of the DC-coupled electric vehicle (EV) charging stations. The scheme provides DC-link voltage regulation while coordinating the charging activities of multiple EVs and integrating battery energy storage systems (BESSs), supercapacitors, renewable energy sources, and a bidirectional voltage source inverter (B-VSI). While existing inertial droop-based control strategies require measurements of the DC-source output power to tune their response according to the assigned inertia, the proposed S-PSC relies solely on DC-link voltage measurements to decouple the DC power demand into multiple inertia-response levels. The S-shaped function prioritizes the compensation of these response levels by dynamically coordinating the operation of the B-VSI, BESS, and EV storage units, ensuring acceptable state of charge, adequate inertia support, and operation close to nominal power levels. A small-signal analysis confirms voltage stability and attenuation of the BESS current. Experimental validation using hardware-in-the-loop under 60 min of intensive EV charging during peak hour demonstrated that the S-PSC reduces BESS stress by 40%, increases energy delivery to EVs by 32%, enhances the economic benefit of BESS utilization, and mitigates flicker in the low-voltage grid when compared with the conventional benchmark solution for industrial applications.

INDEX TERMS Electric vehicle (EV) charger, DC-coupled charging station (CS), renewable energies, battery energy storage system (BESS), secondary level control, hardware-in-the-loop (HIL).

I. INTRODUCTION

The growth of renewable energy generation has driven the adoption of grid-connected battery energy storage systems (BESSs) and charging stations (CSs) to provide grid support. In this context, the automotive industry is gradually electrifying its fleet, further reinforcing the need for clean energy generation to supply the charging demand of electric vehicles (EVs). However, several challenges remain for widespread adoption, including battery lifespan, the impact of intermittent renewable generation on the grid, and instabilities caused by the integration of large numbers of fast EV chargers (FEVCs) and medium EV chargers (MEVCs) to low-voltage networks [1].

Some of these issues have been discussed in [2], which analyzes the voltage fluctuations induced by FEVCs under high renewable penetration, as well as load current variations during EV charging start and stop events. Other studies investigate the stability reduction in low-voltage AC distribution networks when multiple power converters operate in parallel at a common AC-link [3], largely attributed to high harmonic distortion [4].

Solutions based on DC-coupled EV charging station (DC-EVCS) are considered an effective option to mitigate grid voltage fluctuations and reduce the number of AC/DC bidirectional converters connected in parallel to the AC-link. Compared with conventional grid-connected CS, the DC-EVCS

has less stage for power conversion and avoids frequency stability issues [5]. This makes it more suitable for high-power distribution systems integrating photovoltaic (PV), wind turbines (WTs), fuel cells, and BESS, thereby enhancing the scalability of charging infrastructures [6].

One potential advantage of this infrastructure is the ability to exploit the diversification of DC power units [7]. Several studies have proposed integrating renewable energy sources, such as PV–BESS systems with CSs [8]. Others have explored the use of CSs to provide ancillary services, including voltage support in DC microgrids [9] and stability enhancement in AC grids [10], [11]. Moreover, emerging solutions are considering the use of supercapacitors (SCs) for ancillary service provision [12], [13]. Advances in hybrid energy storage systems for EVs [14] have also raised interest in leveraging SCs to improve overall power quality, which constitutes one of the key motivations of this work.

In DC-EVCS infrastructures, significant research efforts are directed toward developing rigid power-sharing control (PSC) strategies that account for all available power units connected to the DC-link, including CSs, BESSs, renewable sources, ancillary services, and grid interfaces. The PSC coordinates these units to maximize efficiency and maintain power quality [15]. Therefore, a high-level control layer is required to adapt the operation of the sources according to energy availability, energy storage state of charge (SoC), and grid condition.

One of the main purpose of the high-level control is to enable an intelligent and adaptable power control among the multiple power converters connected to the DC-link. In [15], a tertiary control layer was proposed to smooth power flow between FEVCs and the utility grid. However, this method focuses solely on enhancing EV charging functionalities and grid support, without addressing BESS degradation or renewable sources fluctuations. In a different direction, Khalid and Panigrahi [16] developed a decentralized power management strategy for multi-BESS-PV system with SoC balancing. In this solution, a power sharing ratio was implemented to coordinate the power exchange between the BESS and the utility grid. Under grid-connected operation, the emphasis was placed on enhancing grid support, without considering the impact on multi-BESS performance under high power deficit conditions.

Moreover, for EV charging applications, ensuring DC-link voltage regulation is crucial, as it is strongly affected by the intermittency of renewable energy sources and load variations. Therefore, Mahfouz and Iravani[10] suggested a BESS-connected CS. Although this approach enhances the stability level, designing a BESS to withstand high voltage levels poses a challenge. Furthermore, this scheme limits BESS controllability, causing operation under extreme power conditions and accelerating battery deterioration.

To improve the BESS lifespan, other solutions have proposed interconnecting all them through dedicated power converters. For instance, Khalid and Panigrahi [16] introduced a line-compensated P–V inertial droop-based PSC for DC-link voltage regulation, while Sharida [15] employed a proportional–integral controller to regulate the DC-link through bidirectional AC–DC converters. Although both methods achieve DC-link voltage regulation, the PSCs presented in these studies limit flexibility in determining optimal power references for BESSs, CSs, and bidirectional AC/DC converters. Consequently, they require additional control structures and measurements to achieve efficient power coordination, particularly when prioritizing BESS lifespan.

Given the growing interest in managing SC energy to provide ancillary services, several studies have proposed using SCs to support BESSs and extend their lifespan. In [12], a PSC for an ultrafast charger was presented. Although this solution achieves DC-link voltage regulation and improves transient response, it does not address the integration of ancillary services nor the stability under different operating modes with respect to BESS and SC SoCs. To address these challenges, the authors in [14] and [17] proposed an energy management system based on an S-shaped function, which provides efficient power coordination between SC and batteries while ensuring stability under critical SoC conditions. Although these strategies were implemented in hybrid EV powertrains, their use on the S-shaped function as a high-level power coordination tool is particular relevance to this work.

The use of nonlinear S-shaped functions is particularly relevant for handling mode transitions in energy storage systems, such as variations in SoC levels and power demands [18], [19]. Owing to their smooth and continuous characteristics, being of class C^{∞}, these functions are well-suited for integration into power-sharing strategies in DC-EVCSs. This class of functions encompasses sigmoid, hyperbolic tangent (tanh), and even third-order polynomial functions. They meet the DC-link voltage fluctuations as soon as possible when the operating point is close to nominal conditions, while reshaping the droop curve to smooth the response as the output power approaches the upper or lower limits of source capacity [20].

Based on the aforementioned ideas, this work proposes the use of S-shaped functions to reshape droop curves and manage energy flow among BESSs, FEVCs, MEVCs, and AC–DC bidirectional converters. The proposed S-shaped-based PSC (S-PSC) prioritizes DC-link voltage regulation, EV charging quality, BESS state of health (SoH), and flicker reduction at the grid bus. Furthermore, the strategy accounts for the intermittent nature of renewable sources and leverages EV batteries and SCs to provide ancillary services, while ensuring stability under critical operating conditions. The main contributions of this work are summarized as follows.

1) A high level control scheme for DC-EVCS to manage multiple DC-coupled sources with different inertia level, exploiting the best power and time-response characteristics of each unit.
2) Flexibility and stability in operating a diverse set of DC-coupled sources, including EVs with different battery and SC characteristics.

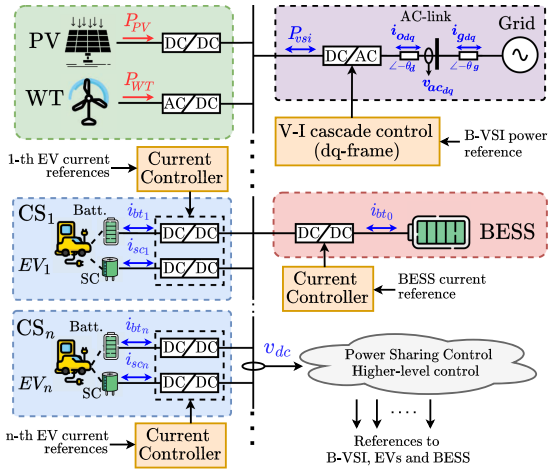

FIGURE 1. DC-EVCS case study.

3) Extension of BESS lifespan by smoothing dynamic responses and promoting gradual power-mode transitions as a function of SoC level.
4) Enhancement of ancillary service provision on the DC-side, while smoothing the transient response of the AC–DC bidirectional converter.

The rest of this article is organized as follows. Section II describes the DC-EVCS case study. Section III introduces the proposed S-PSC. Section IV presents the small-signal stability and performance analysis. Sections V and VI report, respectively, the simulation and experimental results and discuss the effectiveness of the proposed method. Finally, Section VII concludes this article and outlines potential directions for future work.

Notations: The sets $\mathbb{R}$, $\mathbb{R}_+$, and $\mathbb{R}_+^*$ denotes the set of real numbers, nonnegative real numbers, and strictly positive real numbers, respectively. The symbol $(\cdot)^T$ indicates the transpose of vectors and matrices, $\hat{(\cdot)}$ indicates the small signal value of a signal, and $\nabla_{\boldsymbol{x}}(\cdot)$ is the gradient operator in respect to $\boldsymbol{x}$. The vector $\boldsymbol{x_{dq}} = [x_d\ x_q]^T$ denotes the d-axis and q-axis components associated with the variable x.

II. AC AND DC-SIDE COUPLING MODELING

Fig. 1 illustrates the DC-EVCS used as the case of study. On the AC-side, a bidirectional voltage source inverter (B-VSI) provides the interlinking between the DC and AC voltages, while the AC-link serves as the common coupling point for the AC generators.

On the DC-side, the DC-link integrates the PV, WT, BESS, MEVCs, and FEVCs. The CSs have n slots for charging plug-in hybrid and/or EV models. In addition, this case study, the authors are considering that all EV models include an SC as an auxiliary source.

A. AC-SIDE COUPLING

The AC-link voltage in the synchronous reference frame is used to estimate the local power quality of the AC-side. In this context, its voltage $\boldsymbol{v}_{\mathbf{ac}_{dq}}$ and frequency, denoted by ω_{ac}, are calculated as follows:

$$\boldsymbol{v}_{\mathbf{ac}_{dq}} = (R_n + k_{rn}u_2)\left(\boldsymbol{T}\left(-\theta_d\right)\boldsymbol{i}_{\boldsymbol{o}_{dq}} + \boldsymbol{T}\left(-\theta_g\right)\boldsymbol{i}_{\boldsymbol{g}_{dq}}\right) \tag{1a}$$

$$\omega_{\text{ac}} = \omega_g + \frac{v_{\text{ac}_q}}{v_{\text{ac}_d}} \tag{1b}$$

where R_n is defined as the coupling resistor of the AC-link, u_2 represents the active load disturbances on the AC-side, and k_{rn} is the DC gain of the disturbance. The phase angles of the B-VSI output and the grid with respect to the AC-link are defined as θ_d and θ_g, respectively.

In addition, $\boldsymbol{i}_{\boldsymbol{o}_{dq}}$ and $\boldsymbol{i}_{\boldsymbol{g}_{dq}}$ are the currents flowing through the second inductor of the B-VSI output filter and the grid, respectively. In (1b), ω_g is the grid frequency, while v_{ac_d} and v_{ac_q} are the dq components of the $\boldsymbol{v}_{\mathbf{ac}_{dq}}$ vector.

Definition 1: The operator used to shift the dq reference frame with respect to the phase angle θ at different points of connection is defined as

$$\boldsymbol{T}(\theta) = \begin{bmatrix} \cos(\theta) & \sin(\theta) \\ -\sin(\theta) & \cos(\theta) \end{bmatrix}. \tag{2}$$

B. DC-SIDE COUPLING

The dynamics of the DC-link voltage, denoted by v_{dc}, is defined from the sum of the output currents of each coupled converter, as follows:

$$\dot{v}_{\text{dc}} = \left(P_{\text{PV}} + P_{\text{WT}} - P_{\text{vsi}} + k_{\text{dc}}u_1\right) v_{\text{dc}}^{-1} C_{\text{dc}}^{-1} + \ldots$$
$$\ldots + \left(\sum_{i=0}^{n} d_{\text{bt}_i} i_{\text{bt}_i} + \sum_{i=1}^{n} d_{\text{sc}_i} i_{\text{sc}_i}\right) C_{\text{dc}}^{-1} \tag{3}$$

where i_{bt_i} and i_{sc_i} are the ith battery and SC currents, d_{bt_i} and d_{sc_i} are the ith control signal of their respective converters, P_{PV}, P_{WT}, and P_{vsi} are the power of the PV, WT, and B-VSI, respectively, C_{dc} is the capacitance of the DC-link, and u_1 represents the power disturbances from the PV and WT, with k_{dc} being the DC gain of this disturbance. The index $i = 0$ refers to the BESS, while $i = 1, 2, \ldots, n$ refers to the ith EV connected to the CS.

III. PROPOSED S-SHAPED-BASED POWER SHARING CONTROL

The proposed S-PSC aims primarily to reduce the degradation of the BESSs connected to the system, without compromising the power quality of the AC distribution grid. This is achieved through the following operations.

1) A four-band frequency decomposition separates the power demand into virtual-inertia components and high-frequency damping term, enabling coordinated energy sharing among the BESS, the B-VSI, and the EV sources.
2) The B-VSI active power control receives the low-frequency (high-inertia) power reference.
3) The BESS current control receives power references across all inertia levels and prioritizes compensating each one according to its SoC.

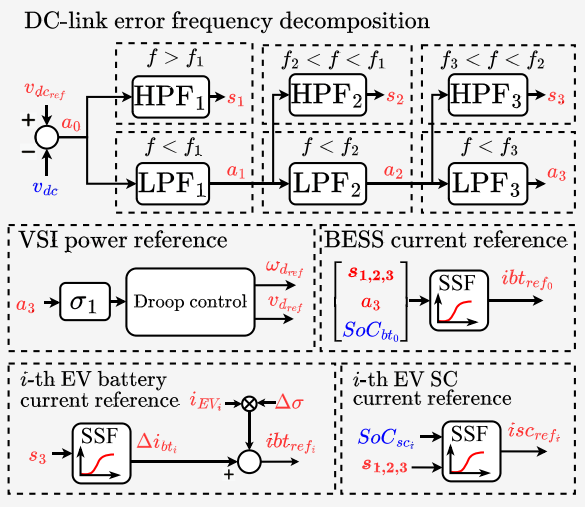

FIGURE 2. Block scheme of the proposed S-PSC.

4) The SC units connected to the EVs are used to compensate high-frequency (low-inertia) power demands, thereby reducing voltage fluctuations on the DC-link.
5) The EV batteries also contribute to compensating moderate-inertia responses on the DC-link. Furthermore, the EVs reduce their charging power to enhance stability under weak-grid conditions.

A. DC-LINK ERROR FREQUENCY DECOMPOSITION

The error between the DC-link voltage reference $v_{\mathrm{dc_{ref}}}$ and the actual voltage v_{dc} serves as an indicator of the power demand required for DC-link voltage regulation. This error, denoted as a_0, is decomposed into different spectral components using three pairs of linear filters, each consisting of a high-pass filter (HPF) and a low-pass filter (LPF), as illustrated in Fig. 2. Consequently, the resulting spectral bands can be interpreted as analogous to inertia contributions in a rotational generation system formed by multiple renewable sources, where the BESS and SC units provide virtual inertial behavior by partially processing energy transients on the DC-link through power reference decoupling [21].

1) HPF AND LPF DYNAMICS

Each filter pair separates a_0 into a high-frequency component (s_k) and a low-frequency component (a_k), whose dynamics are defined as

$$\dot{x}_k = \underbrace{\left(a_{k-1} - x_k\right)}_{s_k} f_k \tag{4a}$$

$$\dot{a}_k = \left(a_{k-1} - a_k\right) f_k \tag{4b}$$

where x_k, with $k = 1, 2, 3$, represents the kth washout state, and f_k denotes the kth cutoff frequency of the corresponding filter pair, satisfying $f_1 > f_2 > f_3$. As a result, six spectral components are obtained. In the control structure, three high-frequency bandwidths are grouped as $\boldsymbol{s_{1,2,3}} = [s_1 \ s_2 \ s_3]^T$, while the low-frequency component is represented by a_3. Together, these signals preserve the full spectral content of the original error signal a_0.

2) VIRTUAL INERTIA AND POWER REFERENCE DECOUPLING

The power reference for DC-link voltage compensation is obtained as the sum of the filtered current references, denoted by i_{ref_r} for $r = 1, 2, 3, 4$. Each i_{ref_r} is associated with a specific spectral component given by $\boldsymbol{s_{1,2,3}}$ and a_3. Consequently, the DC-link voltage error dynamics can be expressed as follows:

$$\underbrace{a_0 k_1 \mathrm{HPF}_1}_{=i_{\mathrm{ref}_1}} + \underbrace{a_0 k_2 \mathrm{LPF}_1 \mathrm{HPF}_2}_{=i_{\mathrm{ref}_2}} + + \underbrace{a_0 k_3 \mathrm{LPF}_2 \mathrm{HPF}_3}_{=i_{\mathrm{ref}_3}} + \underbrace{a_0 k_4 \mathrm{LPF}_3}_{=i_{\mathrm{ref}_4}} = \sum_{r=1}^{4} i_{\mathrm{ref}_r} \tag{5a}$$

$$\dot{a}_0 = \underbrace{\frac{1}{k_1}\dot{i}_{\mathrm{ref}_1} + \frac{f_1}{k_1} i_{\mathrm{ref}_1}}_{\text{Power decoupling for } s_1} \tag{5b}$$

$$\dot{a}_0 = \underbrace{\frac{1}{k_2 f_1}\ddot{i}_{\mathrm{ref}_2} + \frac{(f_1 + f_2)}{k_2 f_1}\dot{i}_{\mathrm{ref}_2} + \frac{f_2}{k_2} i_{\mathrm{ref}_2}}_{\text{Power decoupling for } s_2} \tag{5c}$$

$$\dot{a}_0 = \underbrace{\frac{1}{k_3 f_2}\ddot{i}_{\mathrm{ref}_3} + \frac{(f_2 + f_3)}{k_3 f_2}\dot{i}_{\mathrm{ref}_3} + \frac{f_3}{k_3} i_{\mathrm{ref}_3}}_{\text{Power decoupling for } s_3} \tag{5d}$$

$$\dot{a}_0 = \underbrace{\frac{1}{k_4 f_3}\ddot{i}_{\mathrm{ref}_4} + \frac{1}{k_4}\dot{i}_{\mathrm{ref}_4}}_{\text{Power decoupling for } a_3} \tag{5e}$$

where k_r is the proportional gain (or S-shaped steepness) associated with the respective spectral component, and HPF_k and LPF_k are the filters associated with the cutoff frequency f_k. Therefore, the variation of a_0 is governed by the dynamics of i_{ref_r}, in which the power decoupling is intrinsically linked to the corresponding DC-link spectral frequency components. Moreover, the second-order derivative terms introduce virtual inertia, while the first-order derivative terms provide virtual damping, thereby enabling selective transient energy exchange among the DC power units.

B. VSI POWER CONTROL

A high-inertia emulation in the B-VSI is effective for mitigating voltage fluctuations on the AC-side. Since a_3 represents the low-frequency response, it is used as the reference signal for a conventional droop-based active power control of the B-VSI. Thus, the active (calculated according to the AC-side frequency $\omega_{d_{\mathrm{ref}}}$) and reactive power references (based on the dq AC-side voltage $v_{d_{\mathrm{ref}}}$) are determined by the following droop control model:

$$\omega_{d_{\mathrm{ref}}} = \omega_g - m_d\left(\sigma_1 a_3 + P_{\mathrm{vsi}}\right) \tag{6a}$$

$$v_{d_{\mathrm{ref}}} = v_g - n_d Q_{\mathrm{vsi}} \tag{6b}$$

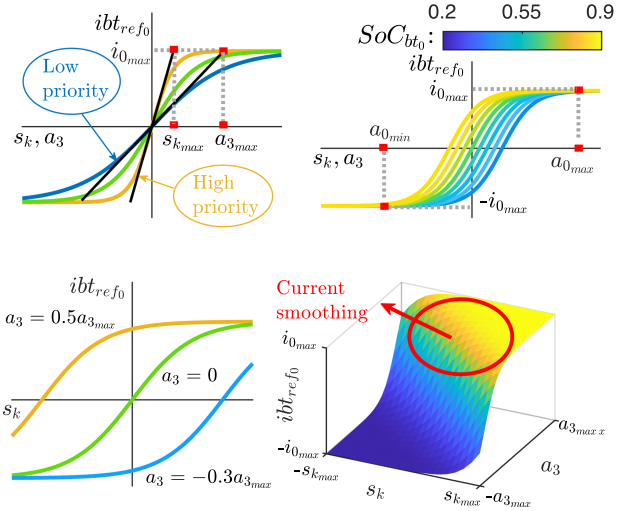

FIGURE 3. BESS current reference. (a) S-shaped design according to DC-link regulation power demand priority. (b) S-shaped adjustment according to SoC_{bt_0} variation. (c) and (d) Behavior of ibt_{ref_0} in terms to s_k and a_3.

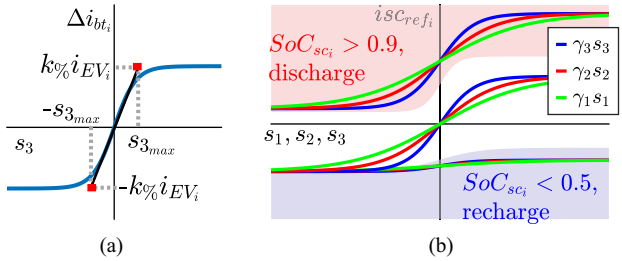

FIGURE 4. EV current references. (a) S-shaped design for battery current reference. (b) S-shaped design for SC current reference under variation of three terms: $\gamma_1 s_1$, $\gamma_2 s_2$, and $\gamma_3 s_3$.

where Q_{vsi} denotes the reactive power of the B-VSI, $\sigma_1 = \frac{v_{\text{dc}_{\max}} - v_{\text{dc}_{\min}}}{P_{\max}}$, $m_d = \frac{2\pi(f_{\max} - f_{\min})}{P_{\max}}$, and $n_d = \frac{v_{\text{ac}_{\max}} - v_{\text{ac}_{\min}}}{Q_{\max}}$.

Here, $P_{\max}$ and $Q_{\max}$ are the maximum active and reactive power of the B-VSI; $v_{\text{dc}_{\max}}$ and $v_{\text{dc}_{\min}}$ are the maximum and minimum DC-link voltages; and $f_{\max}$, $f_{\min}$, $v_{\text{ac}_{\max}}$, and $v_{\text{ac}_{\min}}$ are the maximum and minimum frequency and AC-link voltages, respectively.

C. BESS CURRENT CONTROLLER

The BESS must be designed with sufficient capacity to supply energy during peak hours, while prioritizing energy storage during off-peak periods. Its power\current reference ibt_{ref_0} is generated using an S-shaped function, given as

$$ibt_{\text{ref}_0} = \frac{2i_{0_{\max}}}{1 + \exp^{-[\boldsymbol{\gamma}\ \sigma_2]\times \begin{bmatrix} \boldsymbol{s_{1,2,3}} \\ a_3 \\ \Delta \text{SoC}_{\text{bt}_0} \end{bmatrix}}} - i_{0_{\max}}$$

where $\boldsymbol{\gamma} = [\gamma_1\ \gamma_2\ \gamma_3\ \gamma_4] \in \mathbb{R}^+ \mid \ldots$

$$\ldots \gamma_1 = \frac{2}{s_{1_{\max}}},\ \gamma_2 = \frac{2}{s_{2_{\max}}},\ \gamma_3 = \frac{2}{s_{3_{\max}}},\ \gamma_4 = \frac{2}{a_{3_{\max}}} \quad (7)$$

where $i_{0_{\max}} \in \mathbb{R}^+$ is the maximum BESS current, $\boldsymbol{\gamma}$ is the set of steepness coefficients used to determine the variations of s_k and a_3 with the terms $s_{k_{\max}}$ and $a_{3_{\max}} \in \mathbb{R}^+$ denoting the maximum values of s_k and a_3, respectively.

The selection of $s_{k_{\max}}$ and $a_{3_{\max}}$ determines the priority for compensating the power demands associated with the decomposed spectral components [see Fig. 3(a)]. The procedure for selecting $\boldsymbol{\gamma}$ is detailed in Appendix A.

Remark 1: As s_1 contains the highest spectral components, $s_{1_{\max}}$ must assume larger values to mitigate not only high-frequency resonances but also the propagation of ripple from the DC-connected devices.

As discussed in [14] and [17], operating the battery at extreme SoC levels (e.g., 20% or 80%) increases its internal resistance. To prevent such operation and minimize losses, the term $\sigma_2 \Delta \text{SoC}_{\text{bt}_0}$ was introduced in the function, where $\sigma_2 \in \mathbb{R}^+$ and $\Delta \text{SoC}_{\text{bt}_0} = \text{SoC}_{\text{bt}_0} - \text{SoC}_{\text{bt}_{\text{ref}}}$.

Thus, when the SoC falls below to the threshold $\text{SoC}_{\text{bt}_{\text{ref}}}$, the S-curve shifts to the right, while for SoC values above $\text{SoC}_{\text{bt}_{\text{ref}}}$, it shifts to the left [see Fig. 3(b) for $\text{SoC}_{\text{bt}_{\text{ref}}} = 0.6$]. The gain σ_2 establishes the priority of SoC regulation and can be tuned according to grid conditions and period of day.

Moreover, as a_3 increases or decreases, the S-shaped function smooths the current reference used to track the other spectral components [see Fig. 3(c) and (d)]. These conditions attenuate BESS current variations during critical power operations, thereby mitigating stresses caused by overload and excessive heat generation.

D. EV CURRENT CONTROLLERS

In this study, the EV charges its battery while simultaneously contributing to the mitigation of voltage fluctuations occurring in the medium-frequency spectral range. This strategy improves DC-side power quality without imposing significant stress on the EV batteries.

1) EV BATTERY CURRENT CONTROLLER

The charging process consists of two main steps: 1) constant-current (CC) mode, applied when the SoC is above 20% until it reaches approximately 70%–80%; and 2) constant-voltage (CV) mode, applied thereafter. Furthermore, to enable the ith EV to contribute to DC-link voltage regulation under moderate spectral components, the CC mode is augmented with the sigmoid function shown in Fig. 4(a), expressed as

$$\Delta i_{\text{bt}_i} = \frac{2i_{\text{EV}_i} k_{\%}}{1 + \exp^{-\gamma_3 s_3}} - i_{\text{EV}_i} k_{\%} \quad (8)$$

where $i_{\text{EV}_i} \in \mathbb{R}^+$ is the charging current of the ith EV, and $k_{\%} \in [0, 0.2]$ is a contribution factor of i_{EV_i} used to support s_3 regulation.

Under weak grid conditions, intensive EV arrivals at the DC-EVCS can lead to significant AC-link voltage fluctuations. Therefore, reduced power bounds must be imposed on the B-VSI to avoid instabilities on the AC side. Consequently, the DC side loses part of the B-VSI capacity for EV energy provision and may need to operate in islanded mode.

To ensure continuous operation, the EV charging power is adjusted according to the factor expressed as follows:

$$\Delta\sigma = \frac{1}{1+\exp^{(a_3 - a_{0_{\max}})}}. \tag{9}$$

The limited energy provision capability of the B-VSI causes the DC-link voltage error to increase until it reaches the threshold $a_{0_{\max}}$. Once this threshold is exceeded, the EV charging power demand is curtailed, while the BESS and renewable sources continue supplying energy to the DC-link, thereby ensuring continuous system operation.

2) SC CURRENT CONTROLLER

The high power density of SCs allows them to compensate load fluctuations associated with high spectral components (low inertia), thereby providing ancillary services that enhance the power quality of the grid. Accordingly, the required current is_i is determined as a function of $\boldsymbol{s_{1,2,3}}$, as follows:

$$is_i = \frac{2is_{i_{\max}}}{1+\exp^{-[\gamma_1\ \gamma_2\ \gamma_3]\times \boldsymbol{s_{1,2,3}}}} - is_{i_{\max}} \tag{10}$$

where $is_{i_{\max}} \in \mathbb{R}^+$ is the maximum discharge/recharge current of the SCs.

The SCs must meet safety specifications to prevent thermal runaway risks. Therefore, motivated by [14], (10) is extended with additional S-functions to ensure SC operation within a safe range of 50%–90% SoC, thus avoiding overload conditions. Specifically, when $0.5 < \text{SoC}_{\text{sc}_i} < 0.9$, the SCs operate according to (10). Conversely, when $\text{SoC}_{\text{sc}_i} < 0.5$ or $\text{SoC}_{\text{sc}_i} > 0.9$, the SCs are forced to recharge or discharge, respectively. The expected current reference isc_{ref_i} is illustrated in Fig. 4(b), and its analytical expression is given by

$$isc_{\text{ref}_i} = \frac{1.5is_{i_{\max}}}{1+\exp^{100(0.9-\text{SoC}_{\text{sc}_i})}} + \ldots$$
$$\ldots + \frac{is_i + is_{i_{\max}}}{1+\exp^{100(\text{SoC}_{\text{sc}_i}-0.5)}} - is_{i_{\max}}. \tag{11}$$

IV. STABILITY AND PERFORMANCE ANALYSIS

The stability of the proposed power-sharing strategy is evaluated by using the small-signal Lyapunov's indirect method, as described in [14]. First, the dynamic equations of the DC-EVCS are combined with the previously modeled S-PSC and linearized in Section IV-A. Then, in Section IV-B, the Jacobian matrix is used to analyze the eigenvalue trajectories as the short-circuit ratio (SCR) varies. Finally, Section IV-C examines the attenuation performance of the battery currents and DC-link voltage under the S-PSC through singular-value analysis.

TABLE 1. DC-Coupled EV CS Electrical Parameters

Description	Symbol	Value
AC-side		
LCL input	L_l; R_l	0.3 mH; 20 mΩ
LCL capacitance	C_o; R_d	50 μF; 3 Ω
LCL output	L_o; R_o	0.8 mH; 0.1 Ω
Grid rms voltage	v_g	270 V
Grid frequency	ω_g	$2\pi.50$ rad.s^{-1}
Coupling resistance	R_n	100 Ω
Line impedance (SCR = 6)	L_g; R_g	0.4 mH; 30 mΩ
DC-side		
DC-link rated voltage	$v_{dc_{ref}}$	1000 V
DC-link capacitance	C_{dc}	6000 μF
Converter inductance	L_{bt_i}; L_{sc_i}	5 mH; 5 mH
Converter losses	R_{bt_i}; R_{sc_i}	1 Ω; 1 Ω
BESS voltage	v_{bt_0}	500 V
BESS capacity	C_{bt_0}	56 Ah
1st battery voltage	v_{bt_1}	600 V
1st SC rated voltage	v_{scr_1}	500 V
1st SC capacitance	C_{sc_i}	7 F
2nd to 4th battery voltage	$v_{bt_2} - v_{bt_4}$	600 V
2nd to 4th SC rated voltage	$v_{scr_2} - v_{scr_4}$	450 V
2nd to 4th SC capacitance	$C_{sc_2} - C_{sc_4}$	2 F

A. COUPLING MODEL LINEARIZATION

Let $\boldsymbol{F(x,u)} = \dot{\boldsymbol{x}}$ denote the vector of nonlinear differential equations obtained from the interaction among the main dynamics states presented in Appendix B, where $\boldsymbol{x}$ is the state vector and $\boldsymbol{u}$ is the input vector of $\boldsymbol{F}$. The electrical and control parameters used in the proposed solution are presented in Tables 1 and 2.

Definition 2: The set of solutions $\boldsymbol{x^*}$ and $\boldsymbol{u^*}$, such as $\boldsymbol{F(x,u)}|_{\boldsymbol{x,u=x^*,u^*}} = 0$, is defined as the equilibrium points. These points are computed using MATLABand Simulink [22].

Remark 2: During the computation of the equilibrium points, the most critical scenario was considered, in which the renewable energy generation is null and the CSs demand the maximum power from the utility grid. Therefore, the BESS and the B-VSI operate with higher power requirements, reducing damper effects in both DC and AC-sides.

Assumption 1: The batteries have sufficient capacity such that their SoC dynamics can be neglected. Moreover, since the S-PSC forces the BESS to operate around 60% SoC, this value was assumed as the equilibrium point. Although v_{bt_0} varies with power and SoC fluctuations, it does not substantially affect the eigenvalue trajectories.

Based on the aforementioned considerations, the nonlinear model $\boldsymbol{F(x,u)}$ is linearized around $\boldsymbol{x^*}$ for small-signal variations, denoted by $\hat{\boldsymbol{x}}$. Its dynamics is then obtained through a Taylor series approximation, as follows:

$$\boldsymbol{f}(\hat{\boldsymbol{x}} + \boldsymbol{x^*}, \hat{\boldsymbol{u}} + \boldsymbol{u^*}, t) \approx \boldsymbol{F}(\boldsymbol{x^*}, \boldsymbol{u^*}, t) + \boldsymbol{A}\hat{\boldsymbol{x}} + \boldsymbol{B}\hat{\boldsymbol{u}} \tag{12}$$

TABLE 2. S-PSC Parameters

Description	Symbol	Value
External loop controllers		
Filter frequencies	$[f_1\ f_2\ f_3]$	[100 30 0.1] Hz
Power frequency filter	ω_c	34 rad.s^{-1}
Active power gains	σ_1; m_d;	$2\frac{\text{kW}}{\text{V}}$; 80 $\frac{\mu\text{rad}}{\text{W.s}}$
Reactive power gain	n_d	1 $\frac{\text{mV}}{\text{Var}}$
S-function steepness	γ	[0.06 0.13 0.1 0.06]
BESS SoC regulation	σ_2	8
BESS max. current	$i_{0_{max}}$	100 A;
1^{st} to 4^{th} SC	$is_{1_{max}}$; $is_{2_{max}}$;	80 A; 60 A;
max. current	$is_{3_{max}}$; $is_{3_{max}}$	60 A; 60 A
1^{st} to 4^{th} EV	i_{EV_1}; i_{EV_2};	133 A; 40 A;
max. current	i_{EV_3}; i_{EV_4}	40 A; 40 A
EV contrib. factor	$k_{\%}$	0.1
Inner controllers		
Virtual impedance	R_v; L_v	1 mΩ; 0.1 mH
Feedfoward gains	K_{ffi}; K_{ffv}	0.5; 1
B-VSI voltage loop	K_{pv}; K_{iv}	1.01 S; 123.6 $\frac{\text{S}}{\text{s}}$
B-VSI current loop	K_{pi}; K_{ii}	1.2 Ω; 664 $\frac{\Omega}{\text{s}}$
BESS current loop	$K^0_{bt_p}$; $K^0_{bt_i}$	1 $\frac{\text{m.1}}{\text{A}}$; 1 $\frac{\text{m.1}}{\text{A.s}}$
SC current loop	K_{sc_p}; K_{sc_i}	1 $\frac{\text{m.1}}{\text{A}}$; 1 $\frac{\text{m.1}}{\text{A.s}}$
EV current loop	$K^i_{bt_p}$; $K^i_{bt_i}$	5 $\frac{\text{m.1}}{\text{A}}$; 1 $\frac{\text{m.1}}{\text{A.s}}$

where $\boldsymbol{A}$ is the Jacobian matrix and $\boldsymbol{B}$ is the input matrix, given by

$$\boldsymbol{A} = \nabla_{\boldsymbol{x}} \boldsymbol{F}(\boldsymbol{x}, \boldsymbol{u})|_{\boldsymbol{x},\boldsymbol{u}=\boldsymbol{x}^*,\boldsymbol{u}^*} \in \mathbb{R}^{45\times 45} \tag{13a}$$

$$\boldsymbol{B} = \nabla_{\boldsymbol{u}} \boldsymbol{F}(\boldsymbol{x}, \boldsymbol{u})|_{\boldsymbol{x},\boldsymbol{u}=\boldsymbol{x}^*,\boldsymbol{u}^*} \in \mathbb{R}^{45\times 2}. \tag{13b}$$

B. STABILITY ANALYSIS VARYING SCR

The indirect Lyapunov's method uses $\boldsymbol{A}$ to analyze the local stability of $\boldsymbol{F}(\boldsymbol{x}, \boldsymbol{u})$ through the eigenvalue trajectories.

Assumption 2: In this analysis, we assumed that $\text{SoC}^*_{\text{sc}_i} = 0.5$ or $\text{SoC}^*_{\text{sc}_i} = 0.9$. Ensuring asymptotic stability under these conditions prevents the SCs from drifting into $\text{SoC}_{\text{sc}_i} < 0.5$ or $\text{SoC}_{\text{sc}_i} > 0.9$.

Fig. 5(a) shows the eigenvalue trajectories approaching the right half-plane as the SCR decreases from 6 to 1.2. As expected, under weak grid conditions, the power demand of the loads amplifies the AC-link voltage oscillations, reducing the control stability margin in these scenarios. Nevertheless, the analysis indicates that the overall system is asymptotically stable in SCR > 3, which also ensures that the SoC of the SCs does not drift into $\text{SoC}_{\text{sc}_i} < 0.5$ or $\text{SoC}_{\text{sc}_i} > 0.9$ when disturbances occur.

C. PERFORMANCE ANALYSIS APPLYING DISTURBANCES

The singular values are used to analyze the attenuation performance of $\hat{\boldsymbol{y}} = [\hat{i}_{\text{bt}_0}\ \hat{i}_{\text{bt}_1}\ \hat{i}_{\text{bt}_2}\ \hat{i}_{\text{bt}_3}\ \hat{i}_{\text{bt}_4}\ \hat{v}_{\text{dc}}\ \hat{\theta}_d]^T$ with respect to the load disturbance defined as $\hat{\boldsymbol{u}} = [\hat{u}_2\ \hat{u}_1]^T$. In the same way, the gain output of $\hat{\boldsymbol{y}}$ with respect to $\hat{\boldsymbol{u}}$ was evaluated using the transfer function matrix denoted as $\boldsymbol{H}(s) \in \mathbb{R}^{7\times 2}$

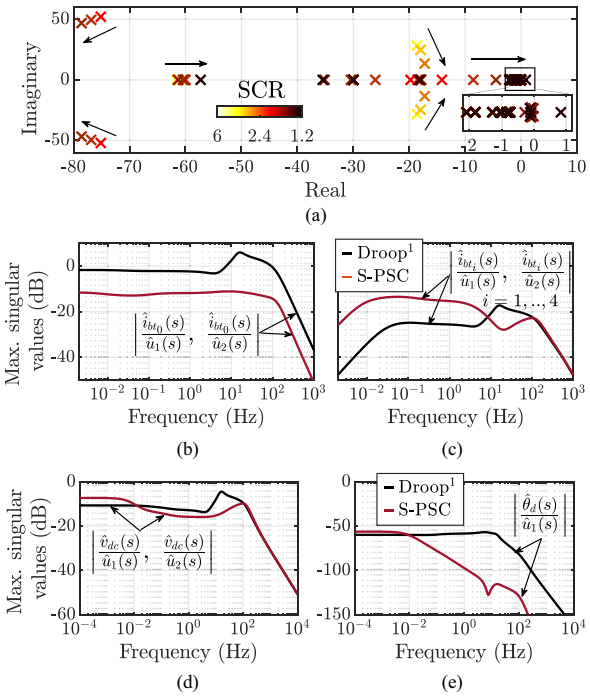

FIGURE 5. Stability and attenuation performance analysis. (a) Low-frequency eigenvalue trajectories with SCR varying from 6 to 1.2; maximum singular values (droop comparison): (b) $\hat{i}_{\text{bt}_0}$ with respect to $\hat{u}_1$ and $\hat{u}_2$, (c) $\hat{i}_{\text{bt}_i} \mid i = 1, 2, 3, 4$ with respect to $\hat{u}_1$ and $\hat{u}_2$, (d) $\hat{v}_{\text{dc}}$ with respect to $\hat{u}_1$ and $\hat{u}_2$, and (e) $\hat{\theta}_d$ with respect to $\hat{u}_1$. [1]The SC units were not included.

calculated by

$$\boldsymbol{H}(s) = \boldsymbol{C}\left(s\boldsymbol{I}^{45\times 45} - \boldsymbol{A}\right)^{-1}\boldsymbol{B} \tag{14}$$

where $\boldsymbol{C} \in \mathbb{R}^{7\times 45}$ is the observation matrix of $\hat{\boldsymbol{y}}$, and $\boldsymbol{I}^{45\times 45}$ is the identity matrix as well.

The singular values were also obtained from the droop-based PSC, which neither accounts the frequency-response decomposition nor employs SCs for DC-link voltage regulation. These values were subsequently compared with those of the proposed solution to more clearly assess its performance attenuation.

Remark 3: During the linearization process, an SCR = 5 was considered. Consequently, the equilibrium points $v^*_{\text{dc}} = 955$ V and $v^*_{\text{ac}_d} = 362$ V were obtained. At these voltage levels, the control structure approaches a low stability margin and the limits of acceptable grid operation. Moreover, under these conditions, the S-shaped function smooths the BESS current reference, which may increase voltage fluctuations at high frequencies.

Remark 4: In this analysis, the range $0.6 < \text{SoC}^*_{\text{sc}_i} < 0.8$ was used. These equilibrium points indicate marginal stability of the overall system due to the absence of SoC_{sc_i} regulation within this operating range [14]. However, these conditions do not move the system into instability and can be useful for investigating the contribution of SCs to BESS current support and DC-link voltage attenuation.

Remark 5: The parameters $k_{rn} = 20$ and $k_{\mathrm{dc}} = 1000$ were defined to amplify the DC gains in $\boldsymbol{H}(s)$, since the load variation occurs on the kilowatt scale. This approach is useful for predicting variations in the battery current and DC-link voltage under high-power demands.

1) BESS CURRENT ATTENUATION PERFORMANCE

Fig. 5(b) shows the singular values of $\hat{i}_{\mathrm{bt}_0}$ with respect to $\hat{u}_1$ and $\hat{u}_2$. The results demonstrate that the proposed S-PSC reduces the BESS current DC gain by more than 15 dB through the ancillary services provided by the SCs and EV batteries. Most of this attenuation is attributed to the SCs, which are specifically employed for this purpose.

In contrast, the EV batteries sustain a higher current magnitude to compensate for the DC-link voltage in the medium-frequency range between 0.01 and 10 Hz, as shown in Fig. 5(c). Although the EV batteries participate in DC-link voltage regulation alongside the BESS, their contribution occurs in frequency ranges that do not significantly affect the BESS lifespan.

2) DC-LINK ATTENUATION PERFORMANCE

The attenuation of DC-link voltage fluctuations under disturbances was analyzed in Fig. 5(d) where, it shows the singular values of $\hat{v}_{\mathrm{dc}}$ with respect to $\hat{u}_1$ and $\hat{u}_2$. In addition, it can be observed that voltage attenuation is more evident in the frequency range above 0.01 Hz, at the cost of a higher DC gain.

This result indicates that the proposed S-PSC can effectively absorb voltage fluctuations caused by the intermittent nature of renewable sources. The increased steady-state error can be attributed to the smoothing characteristic of the sigmoid function, which reduces the compensation of i_{bt_0} with respect to a_3, thereby affecting DC-link voltage steady-state error.

3) B-VSI FREQUENCY ATTENUATION PERFORMANCE

The inertia gain of the B-VSI was also investigated by evaluating the frequency response of $\hat{\theta}_d$ with respect to $\hat{u}_1$. As shown in Fig. 5(e), the proposed S-PSC attenuates high-frequency components above 0.01 Hz, causing the B-VSI to respond more slowly to DC-side load disturbances. This behavior suggests that the proposed solution is a suitable alternative for low-voltage grid applications, as it reduces high-voltage variations in AC-link couplings.

Remark 6: The frequency response with respect to $\hat{u}_2$ was not assessed. Since B-VSI reactive power and harmonics control are not the focus in this work, the effects of $\hat{u}_2$ on the AC-side would not contribute for any deep analysis in the power quality.

V. SIMULATION RESULTS

Simulations were first conducted to validate the proposed S-PSC under diverse grid conditions and varying EV/BESS operating scenarios. For this purpose, data files containing the renewable generation profile and the EV arrival rate were included, as illustrated in Fig. 6(a). Furthermore, $\mathrm{SoC}_{\mathrm{bt}_{\mathrm{ref}}}$ was adjusted according to the daily net load demand, as shown in Fig. 6(b). Consequently, the BESS restores energy during off-peak hours and provides energy support during periods of high load demand.

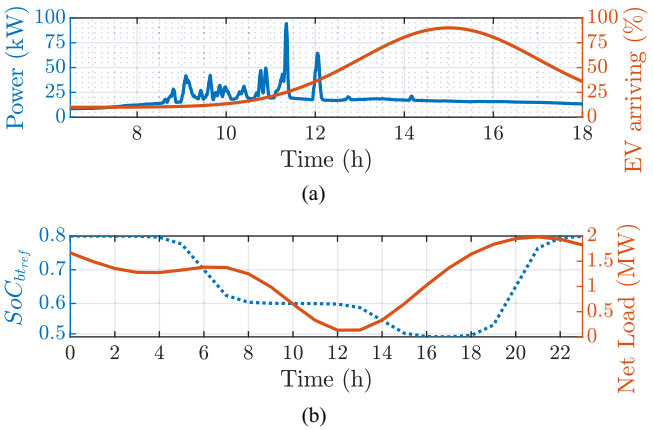

FIGURE 6. Simulation data files. (a) Renewable generation profile and EV arrival rate. (b) BESS $\mathrm{SoC}_{\mathrm{bt}_{\mathrm{ref}}}$ as a function of the daily net load.

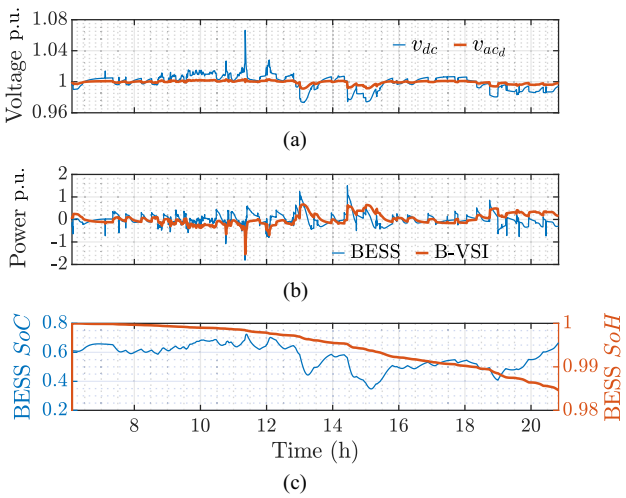

FIGURE 7. S-PSC performance throughout the day. (a) DC-link and AC-link voltage. (b) BESS and B-VSI power. (c) BESS SoC and SoH dynamics.

The model $\boldsymbol{F}(\boldsymbol{x}, \boldsymbol{u})$, BESS dynamics, and their parameters listed in Tables 1 and 2 were discretized in MATLAB and Simulink using the backward Euler method with a minimum time step of 1×10^{-4} s. This discretization captures the dynamic of the S-PSC throughout daily operation and enables a clear stability assessment of the controller gains under different operating conditions.

A. S-PSC PERFORMANCE DURING THE DAY

In this analysis, Fig. 7(a) shows the dynamics of v_{dc} and v_{ac_d} during the period from 6 to 21 h. The largest voltage fluctuations occur on the DC side, where high power density units are

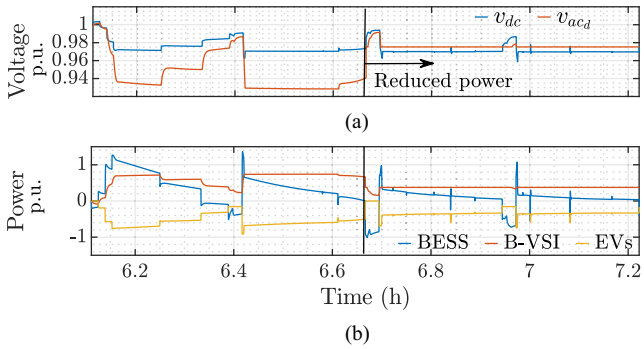

FIGURE 8. S-PSC performance in weak grid condition. (a) DC-link and AC-link voltage. (b) Power processed by the BESS, B-VSI, and EVs.

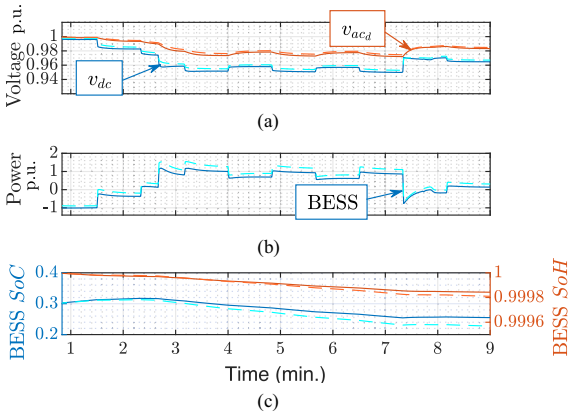

FIGURE 9. Comparison between the proposed S-PSC (continuous line) and the conventional droop control (dashed line). (a) DC-link and AC-link voltage. (b) BESS power. (c) BESS SoC and SoH.

coupled. The DC-side power balance is illustrated in Fig. 7(b), where the BESS supplies energy to sustain all spectral components of the power demand, while the B-VSI contributes only to the low-frequency components. Consequently, the proposed S-PSC ensures reliable operation, with the maximum voltage deviation limited to below 10%.

The simulation results predict the BESS SoC and SoH dynamics throughout the day. As shown in Fig. 7(c), the BESS SoC is maintained within the range of 20% to 80%, with more pronounced variations occurring between 13 and 20 h, mainly due to the higher probability of EV arrivals during this period. In contrast, the SoH is more significantly affected, since it is strongly influenced by the effort required to maintain the SoC within safe operating limits. A solution for reducing SoH degradation is to adjust $\mathrm{SoC}_{\mathrm{bt}_{\mathrm{ref}}}$ or σ_2 in order to smooth the power processed by the BESS.

B. S-PSC PERFORMANCE UNDER WEAK GRID

To assess the adaptability of the S-PSC under weak grid conditions, a simulation was conducted considering SCR = 1.5. As shown in Fig. 8(a) and (b), between 6 and 6.65 h, the high power processed by the B-VSI leads to significant AC-link voltage drops, which are characteristic of weak grid conditions. Therefore, reducing the power delivered by the B-VSI is crucial to avoid blackouts caused by voltage instability. Consequently, after 6.65 h, the B-VSI operates under reduced power, and the proposed S-PSC adapts the operation of the BESS and EVs according to (9) to maintain voltage stability, as illustrated in Fig. 8(a) and (b).

C. BESS PERFORMANCE WITH S-PSC AND OTHER APPROACHES

A comparison of the proposed S-PSC with a conventional inertial droop-based control was conducted in order to assess the benefits of employing S-shaped functions for power-sharing strategies.

The results in Fig. 9(a) confirm that the proposed S-PSC exhibits a higher DC-link voltage error under steady-state operation, as discussed in the stability analysis. In contrast, the S-PSC effectively limits BESS overload during high power demand [see Fig. 9(b)], thereby protecting the device from undesirable SoC excursions and reducing long-term SoH degradation, as evidenced in Fig. 9(c). These advantages arise from the nonlinear characteristics of the sigmoid functions, which reshape the droop gains and mitigate excessive BESS power effort under high demand scenarios.

The nonlinear characteristics of the S-shaped function can be reproduced using fuzzy-logic-based control, resulting in similar power-sharing behavior [23]. However, adapting the gains and base rule to different device characteristics is considerably more complex with this approach. Furthermore, fuzzy-logic control complicates the derivation of an analytical model for small-signal analysis, which constitutes a disadvantage when compared with the proposed S-PSC. Therefore, the S-shaped strategy based on sigmoid functions is a more suitable choice for achieving the objectives of this work, owing to its continuity, reduced tuning complexity, and straightforward mathematical modeling.

VI. HARDWARE-IN-THE-LOOP (HIL) RESULTS

The experimental results was conducted using a real-time HIL platform. The HIL platform integrates SpeedGoat for real-time DC-EVCS emulation and dSPACE for executing the power sharing strategy and the inner controllers, as indicated in Fig. 10.

The schematic illustrating the board connections is presented in Fig. 10. In this setup, the dSPACE1006 multiprocessor system, featuring an AMD Opteron processor, retrieves analog signals from SpeedGoat through the 16-bit A/D board DS2004 and generates digital signals via the digital board DS4004. Subsequently, the measurements related to the DC-EVCS are obtained from SpeedGoat, which is powered by a performance-core Intel Core i3 FPGA 100 k, using the 16-bit analog output board IO110, while the PWM signals are acquired through the digital board IO316.

In the HIL implementation, the controllers were developed using discrete equations based on backward Euler approximation. During the experimental execution, the user manually

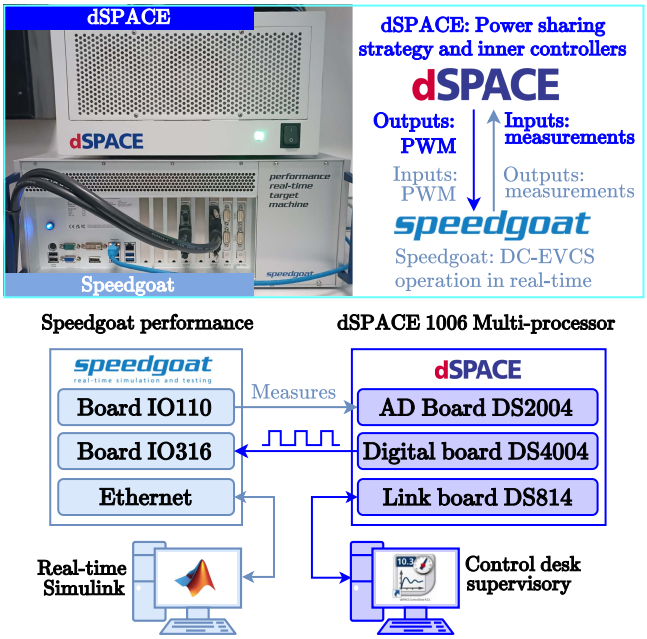

FIGURE 10. Real-time HIL setup: dSPACE and Speedgoat.

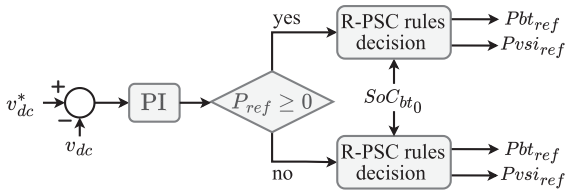

FIGURE 11. Scheme of the R-PSC benchmark solution. Adapted from [16].

TABLE 3. R-PSC Rules Decision. Adapted From [16].

SoC_{bt_0}	above 50%	30-50%	10-30%
$P_{ref} > 0$ (Pbt_{ref}:$Pvsi_{ref}$)	2:1	1:1	1:1.5
$P_{ref} < 0$ (Pbt_{ref}:$Pvsi_{ref}$)	1:2	1:1	1.5:1

set the EV power demands and specified their arrival and departure times at the CSs. For each EV arrival, SoC_{bt_i} and SoC_{sc_i} were reset to random initial conditions within the ranges of 0.2–0.9 and 0.5–0.8, respectively, while the errors in the current control loop were cleared. Furthermore, the battery charging process followed the conventional CC/CV protocol.

Moreover, the proposed S-PSC was compared with the benchmark solution in [16]. The benchmark employs a ratio-based PSC (R-PSC), adapted with the control loop illustrated in Fig. 11, where P_{ref} denotes the power demand, Pbt_{ref} and $Pvsi_{ref}$ represent the battery and B-VSI power references, respectively. The ratio-sharing rules are summarized in Table 3. The R-PSC is designed to operate exclusively in grid-connected mode in peak hours, utilizing a single high-power BESS connected to the DC-link.

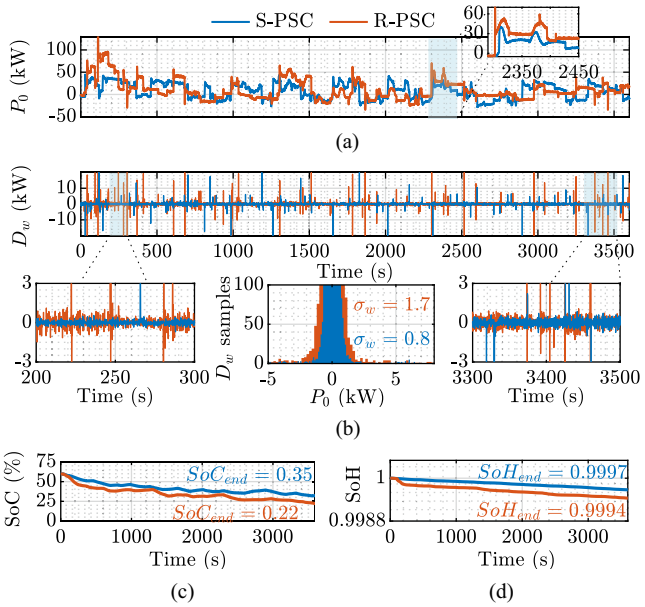

FIGURE 12. BESS performance comparison. (a) BESS Power (P_0). (b) BESS power detail coefficient (D_w) and D_w samples with respect to P_0. (d) SoC. (e) SoH variation.

Finally, the tests were carried out for both strategies under the following conditions: 1) during the test, R_n was varied between 5 and 700 Ω; 2) the power injected by the renewable sources followed the same profile, characterized by high load fluctuations; and 3) in both cases, the grid condition was assumed to represent peak-hour operation with SCR = 6.

A. BESS USAGE

The BESS performance and stress were quantified in terms of power levels, transient responses, SoC, and SoH. With respect to the power response of the R-PSC, the proposed S-PSC not only reduced high-frequency transients in the BESS, but also lowered the rms power for SoC values above 50% [see Fig. 12(a)]. Furthermore, analysis of the BESS power detail coefficient (D_w) obtained via Wavelet Transform and the standard deviation (σ_w) [see Fig. 12(b)] confirms that the proposed strategy results in reduced BESS stress.

In the zoomed intervals of Fig. 12(b), it can be observed that the R-PSC requires greater BESS effort at SoCs above 50%. This behavior results from the abrupt transition of the power-sharing ratio at specific SoC intervals, as shown in Table 3. In contrast, the S-PSC adapts more smoothly to SoC transitions, preventing the BESS from operating under sustained high demand within the same SoC range, as imposed by the R-PSC.

Moreover, the S-PSC demonstrated superior performance in terms of BESS lifespan, as both SoC and SoH were less affected, as shown in Fig. 12(c) and (d). Although the energy sold was less during this time interval, in the long term these results can potentially increase the revenue in 10%–20%. This is further supported by the analysis in Table 4, where the

TABLE 4. BESS Long Term Profit[2] Comparison

	Energy sold	SoC_{end}	SoH_{end}	Profit[1]
R-PSC	13.47 kWh	22.1%	99.94%	2.06 $
S-PSC	12.12 kWh	35.3%	99.97%	2.42 $

[2]Profit calculation is detailed in Appendix C.

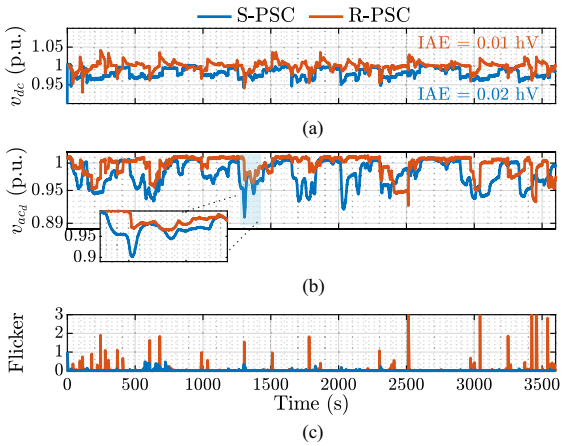

FIGURE 13. Voltage fluctuation comparison. (a) DC-link voltage. (b) AC-link voltage. (c) Instantaneous flicker occurrences.

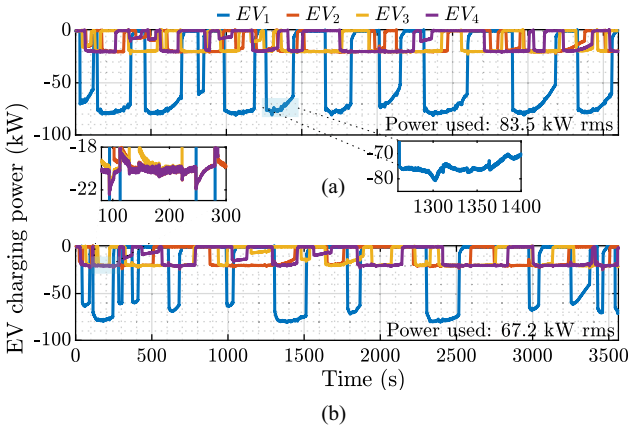

FIGURE 14. EV charging power comparison. (a) S-PSC. (b) R-PSC.

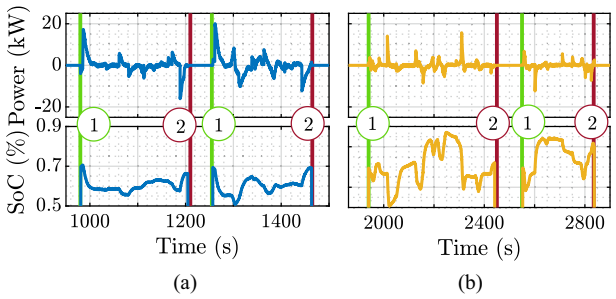

FIGURE 15. SC power and SoC behavior. (a) 1st SC. (b) 3rd SC.

overall cost comparison indicates higher profitability for the S-PSC relative to the R-PSC, taking into account the BESS pack price, SoH degradation, energy sold, and grid energy price.

B. COUPLING POINT VOLTAGE PERFORMANCES

In relation to the DC-link voltage fluctuation, as shown in Fig. 13(a), the S-PSC demonstrated robustness against load disturbances, maintaining the maximum voltage error below 5% throughout the test. However, a higher integral absolute error is expected due to the absence of an integrator in the voltage control loop. Since the voltage error strongly depends on the power distribution between the BESS and the B-VSI, the power-sharing steepness gains must be tuned according to the maximum and minimum DC-link voltage levels of the microgrid.

Fig. 13(b) shows the AC-link voltage fluctuations. The S-PSC influences the low-frequency variations because it requires more energy from the utility grid. Although the AC-link voltage exhibits larger drops, its rms value remains within acceptable limits (IEEE 1159) [24]. Furthermore, these drops occur at low-frequency ranges, thereby mitigating flicker occurrences in accordance with IEEE 1453 [25]. In contrast, the R-PSC results in a higher incidence of flicker [see Fig. 13(c)], which is undesirable for maintaining good power quality in the utility grid.

C. EV CHARGING PERFORMANCE

In the S-PSC, the EV batteries support voltage regulation by compensating medium-spectral frequency components. Fig. 14(a) (zoomed view) highlights the current variations of the EV batteries during connection/disconnection events of the CSs and under power fluctuations of the renewable energy sources. In contrast, the benchmark solution does not provide such support and is therefore more affected by disturbance variations, as shown in the zoomed view of Fig. 14(b).

Moreover, in respect to rms power delivery, exhibited in Fig. 14(a) and (b), the S-PSC with SCs as auxiliary support enabled 34% more power delivery for EV charging during the test. This result attracts the interest in using SCs as complementary sources to improve both power quality and charging performance in the infrastructure.

D. SC PERFORMANCE WITH S-PSC

The SC power dynamics and the corresponding SoC variations were evaluated within a specific time interval, covering the EV plug-in [point ①] and plug-off [point ②] events. Fig. 15(a) illustrates the power processed by the 1st SC, while Fig. 15(b) shows the behavior of the 3rd SC.

As observed, the 1st SC, having higher power density, processed more power compared to the 3rd SC, which has lower power density (smaller capacitance and maximum current). The SC SoC remained within the safe operating limits of 50%–90%, ensuring that the S-PSC provides reliable SC operation avoiding overload conditions and thermal runaway risks.

VII. CONCLUSION

A S-shaped-based power sharing control was proposed in this work for DC-EVCS. The S-shaped function shapes the ratio power of the available source to compensate the DC-voltage across different inertia responses, adapting the operation of BESS and EV energy storage units for ancillary service provision, while ensuring high-inertia responses of the interlinking converter with the utility grid.

The small-signal stability and performance attenuation of the proposed strategy were assessed through eigenvalue trajectory and singular value analyses, respectively. Simulation results predict the controller performance under diverse grid conditions. Furthermore, experimental validation with benchmark comparisons was conducted using an HIL test bench. The results demonstrate that the proposed strategy mitigates flicker and extends BESS lifespan. Compared to a fixed power-sharing ratio without SC support, the S-PSC reduces BESS stress by more than 40% and increases its profit by more than 10%. Nonetheless, a tradeoff arises between extending BESS lifespan and maintaining grid voltage within the acceptable rms tolerance specified by IEEE 1159 [25].

Future work will focus on implementing reactive power sharing control and low voltage ride through support under severe rms voltage drops, indicative of weak grid conditions. In addition, the proposed PSC will be extended to adapt dynamically to changing grid conditions, thereby enhancing power quality on both the DC and AC-sides.

APPENDIX A

In this appendix, the authors demonstrate how to select the S-shaped steepness coefficients $\boldsymbol{\gamma}$ based on the spectral characteristics of the frequency signal used as input.

First, we assume that the reference current follows an S-shaped curve, expressed by the sigmoid function

$$i_{\text{ref}} = \frac{2i_{i_{\max}}}{1+\exp^{-\sum_{j=1}^{k+1}\gamma_j v_j}} - i_{i_{\max}} \tag{15}$$

where γ_j denotes the jth steepness coefficient, k is the number of high-frequency components, and v_j is the jth input signal. The maximum steepness of (15) with respect to v_j is obtained as

$$\left.\frac{di_{\text{ref}}}{dv_j}\right|_{(v_1=0,v_2=0,\ldots,v_{k+1}=0)} = \frac{\gamma_j i_{i_{\max}}}{2} \tag{16}$$

with γ_j defined by

$$\frac{\gamma_j i_{i_{\max}}}{2} = \frac{i_{i_{\max}}}{v_{j_{\max}}} \rightarrow \gamma_j = \frac{2}{v_{j_{\max}}} \tag{17}$$

where the ratio $\frac{i_{i_{\max}}}{v_{j_{\max}}}$ specifies the maximum gain between the current output and the input signal.

APPENDIX B

The remaining differential equations of $\boldsymbol{F(x,u)}$ used in (12) are presented below. The equations was adapted from [14] and [22], and the system parameters adopted in the nonlinear model are summarized in Tables 1 and 2.

LCL dynamics

$$\dot{\theta}_d = \omega_{d_{\text{ref}}} - \omega_{\text{ac}} \tag{18a}$$

$$\dot{\boldsymbol{i}}_{l_{dq}} = \omega_{d_{\text{ref}}}[i_{l_q} - i_{l_d}]^T - \frac{R_l}{L_l}\boldsymbol{i}_{l_{dq}} + \frac{1}{L_l}(\boldsymbol{v}_{\boldsymbol{s_{dq}}} - \boldsymbol{v}_{\boldsymbol{o_{dq}}}) \tag{18b}$$

$$\dot{\boldsymbol{v}}_{o_{dq}} = \omega_{d_{\text{ref}}}[v_{o_q} - v_{o_d}]^T + \frac{1}{C_o}\left(\boldsymbol{i}_{\boldsymbol{l_{dq}}} - \boldsymbol{i}_{\boldsymbol{o_{dq}}}\right) + R_d(\dot{\boldsymbol{i}}_{l_{dq}} - \dot{\boldsymbol{i}}_{o_{dq}}) \tag{18c}$$

$$\dot{\boldsymbol{i}}_{o_{dq}} = \omega_{d_{\text{ref}}}[i_{o_q} - i_{o_d}]^T - \frac{R_o}{L_o}\boldsymbol{i}_{o_{dq}} + \frac{1}{L_o}(\boldsymbol{v}_{\boldsymbol{o_{dq}}} - \boldsymbol{v}_{\boldsymbol{ac_{dq}}}\boldsymbol{T}(\boldsymbol{\theta_d})). \tag{18d}$$

Grid impedance dynamics

$$\dot{\theta}_g = \omega_g - \omega_{\text{ac}} \tag{19a}$$

$$\dot{\boldsymbol{i}}_{g_{dq}} = \omega_g[i_{g_q} - i_{g_d}]^T - \frac{R_g}{L_g}\boldsymbol{i}_{g_{dq}} + \frac{1}{L_g}(\boldsymbol{v}_{\boldsymbol{g_{dq}}} - \boldsymbol{v}_{\boldsymbol{ac_{dq}}}\boldsymbol{T}(\boldsymbol{\theta_g})). \tag{19b}$$

AC–DC converter power dynamics

$$\dot{P}_{\text{vsi}} = \omega_c\left(\frac{3}{2}\left(v_{o_d}i_{o_d} + v_{o_q}i_{o_q}\right) - P_{\text{vsi}}\right) \tag{20a}$$

$$\dot{Q}_{\text{vsi}} = \omega_c\left(\frac{3}{2}\left(v_{o_q}i_{o_d} - v_{o_d}i_{o_q}\right) - Q_{\text{vsi}}\right). \tag{20b}$$

DC–DC converter current dynamics

$$\dot{i}_{\text{bt}_i} = -i_{\text{bt}_i}\frac{R_{\text{bt}_i}}{L_i} + \frac{3v_{\text{bt}_i}}{L_i} - d_{\text{bt}_i}\frac{3v_{\text{dc}}}{L_i} \tag{21a}$$

$$\dot{i}_{\text{sc}_i} = -i_{\text{sc}_i}\frac{R_{\text{sc}_i}}{L_i} + \frac{3v_{\text{sc}_i}}{L_i} - d_{\text{sc}_i}\frac{3v_{\text{dc}}}{L_i}. \tag{21b}$$

SC SoC dynamics

$$\dot{SoC}_{\text{sc}_i} = -\frac{i_{\text{sc}_i}}{C_{\text{sc}_i}v_{\text{scr}_i}}. \tag{22}$$

AC–DC converter zero level control

Virtual impedance:

$$\boldsymbol{v}_{\boldsymbol{o_{dq}}\text{ref}} = [v_{d_{\text{ref}}} \;\; 0]^T - R_v\boldsymbol{i}_{\boldsymbol{o_{dq}}} + \omega_{d_{\text{ref}}}L_v[i_{o_q} \;\; - i_{o_d}]^T. \tag{23a}$$

Voltage loop control:

$$\dot{\boldsymbol{\delta}}_{v_{dq}} = \boldsymbol{v}_{\boldsymbol{o_{dq}ref}} - \boldsymbol{v}_{\boldsymbol{o_{dq}}} \tag{23b}$$

$$\boldsymbol{i}_{\boldsymbol{s_{dq}}} = K_{ffi}\boldsymbol{i}_{\boldsymbol{o_{dq}}} - \omega_{d_{\text{ref}}}C_o[v_{o_q} \;\; - v_{o_d}]^T + K_{pv}\dot{\boldsymbol{\delta}}_{v_{dq}} + K_{iv}\boldsymbol{\delta}_{\boldsymbol{v_{dq}}}. \tag{23c}$$

Current loop control:

$$\dot{\boldsymbol{\delta}}_{i_{dq}} = \boldsymbol{i}_{\boldsymbol{s_{dq}}} - \boldsymbol{i}_{\boldsymbol{l_{dq}}} \tag{23d}$$

$$\boldsymbol{v}_{\boldsymbol{s_{dq}}} = K_{ffv}\boldsymbol{v}_{\boldsymbol{o_{dq}}} - \omega_{d_{\text{ref}}}L_l[i_{l_q} \;\; - i_{l_d}]^T + K_{pi}\dot{\boldsymbol{\delta}}_{i_{dq}} + K_{ii}\boldsymbol{\delta}_{\boldsymbol{i_{dq}}}. \tag{23e}$$

DC–DC converter current control

$$d_{\mathrm{bt}_i} = K^i_{\mathrm{bt}_p}\dot{\delta}_{\mathrm{bt}_i} + K^i_{\mathrm{bt}_i}\delta_{\mathrm{bt}_i},\quad \dot{\delta}_{\mathrm{bt}_i} = i_{\mathrm{bt}_i} - ibt_{\mathrm{ref}_i} \tag{24a}$$

$$d_{\mathrm{sc}_i} = K_{pc}\dot{\delta}_{\mathrm{sc}_i} + K_{ic}\delta_{\mathrm{sc}_i},\quad \dot{\delta}_{\mathrm{sc}_i} = i_{\mathrm{sc}_i} - isc_{\mathrm{ref}_i}. \tag{24b}$$

The main state vector is given by

$$\begin{aligned}\boldsymbol{x} = \big[&\delta_{\mathrm{bt}_0}\ \delta_{\mathrm{bt}_1}\ \delta_{\mathrm{bt}_2}\ \delta_{\mathrm{bt}_3}\ \delta_{\mathrm{bt}_4}\ \delta_{\mathrm{sc}_1}\ \delta_{\mathrm{sc}_2}\ \delta_{\mathrm{sc}_3}\ \delta_{\mathrm{sc}_4}\ \dots\\ &\dots\ \delta_{i_d}\ \delta_{i_q}\ \delta_{v_d}\ \delta_{v_q}\ x_1\ a_1\ x_2\ a_2\ x_3\ a_3\ \mathrm{SoC}_{\mathrm{sc}_1}\dots\\ &\dots\ \mathrm{SoC}_{\mathrm{sc}_2}\ \mathrm{SoC}_{\mathrm{sc}_3}\ \mathrm{SoC}_{\mathrm{sc}_4}\ v_{\mathrm{dc}}\ i_{\mathrm{bt}_0}\ i_{\mathrm{bt}_1}\ i_{\mathrm{bt}_2}\ i_{\mathrm{bt}_3}\dots\\ &\dots\ i_{\mathrm{bt}_4}\ i_{\mathrm{sc}_1}\ i_{\mathrm{sc}_2}\ i_{\mathrm{sc}_3}\ i_{\mathrm{sc}_4}\ \theta_d\ \theta_g\ i_{g_d}\ i_{g_q}\dots\\ &\dots\ i_{o_d}\ i_{o_q}\ v_{o_d}\ v_{o_q}\ i_{l_d}\ i_{l_q}\ P_{\mathrm{vsi}}\ Q_{\mathrm{vsi}}\big]^T\end{aligned} \tag{25}$$

and the nonlinear model is defined as $\boldsymbol{F}(\boldsymbol{x},\boldsymbol{u}) = \dot{\boldsymbol{x}}$.

APPENDIX C

The internal dynamics of the BESS are used to estimate both its SoC and SoH. In this work, the BESS is modeled using a lithium-ion pouch-type cell, adapted from [17] and [26]. The SoC is estimated using the Coulomb's counting method, while the SoH is obtained from a first-order RC equivalent circuit model that captures aging and thermal effects. Accordingly, the SoC and SoH dynamics of the BESS are given by

$$\dot{SoC}_{\mathrm{bt}_0} = -\frac{i_{\mathrm{bt}_0}}{C_{\mathrm{bt}_0}} \tag{26a}$$

$$\dot{SoH} = -\frac{|i_{\mathrm{bt}_0}|}{7,200A_h} \tag{26b}$$

$$A_h = \left[\frac{20}{\Lambda.10^3\exp^{(310c-31,700)/R(T_c+T_s)/2}}\right]^z \tag{26c}$$

where R is the ideal gas constant and z is the power-law factor. Since A_h depends on the cell temperature, its dynamics are also modeled as

$$\dot{T}_s = -\frac{(R_c+R_s)\,T_s}{R_cR_sC_s} + \frac{T_c}{R_cC_s} + \frac{T_f}{R_sC_s} \tag{27a}$$

$$\dot{T}_c = \frac{T_s}{R_cC_c} - \frac{T_c}{R_cC_c} + \frac{Q}{C_c} \tag{27b}$$

$$Q = i_{\mathrm{bt}_0}\left(v_{\mathrm{bt}_0} - v_{oc}(\mathrm{SoC}_{\mathrm{bt}_0})\right) + i_{\mathrm{bt}_0}T_c\frac{\partial v_{oc}(\mathrm{SoC}_{\mathrm{bt}_0})}{\partial T_c} \tag{27c}$$

where T_f is the ambient temperature, and c, R_c, R_s, C_c, and C_s are defined in Tables 5 and 6. Because the heat generation rate depends on the BESS terminal voltage, the electrical dynamics are described by

$$v_{\mathrm{bt}_0} = v_{oc} - R_{op}i_{\mathrm{bt}_0} + v_{rc} \tag{28a}$$

$$\dot{v}_{rc} = \left(R_pi_{\mathrm{bt}_0} - v_{rc}\right)\left(C_0R_p\right)^{-1} \tag{28b}$$

where R_{op}, R_p, C_0, and v_{oc} are also summarized in Tables 5 and 6.

The BESS did not purchase energy from the renewable sources, and it only sold energy to the CSs. Accordingly, the customer's final profit is expressed in terms of the BESS energy sold/purchase and the corresponding battery degradation,

TABLE 5. BESS Model Parameters.

Description	Symbol	Value
BESS capacity	Q_{bt_0}	28 kWh
Polarization capacitor	C_0	15.7 kF
Internal resistances	R_p; R_{op}	Table 6
Open-circuit voltage	v_{oc}	Table 6
Heat conduction	R_c; R_s	182 KW^{-1}; 1,410 KW^{-1}
Thermal capacitances	C_c; C_s	10 kJK^{-1}; 50 kJK^{-1}

Adapted From [17].

TABLE 6. Battery Circuit Parameter Versus SoC, and Pre-Exponential Factor Λ Versus C-Rate.

Description	Symbol				
Battery electrical parameter (single cell) versus SoC					
SoC	SoC_{bt_0}	0.2	0.4	0.6	0.8
Open. voltage	v_{oc}	3.01	3.05	3.15	3.24
Ohmic resist.	R_{op}	0.165	0.145	0.13	0.15
Ionization resist.	R_p	0.046	0.042	0.043	0.045
Pre-exponential factor versus c-rate					
c-rate	c	0.5	2	6	10
Pre-exp. factor	Λ	31.6	21.7	13.9	15.5

Adapted From [17].

as follows:

$$\mathrm{Profit} = E_0\beta_{\mathrm{ch}} - E_g\beta_g - (1-\mathrm{SoH}_{\mathrm{end}})Q_{\mathrm{bt}_0}\beta_0 \tag{29}$$

where E_0 [kWh] denotes the total BESS energy sold, $\beta_{\mathrm{ch}} = 0.32\,\$$ [27] is the charging energy price during peak hours, E_g is the grid energy bought, $\beta_g = 0.12\,\$$ [27], Q_{bt_0} [kWh] is the BESS nominal capacity, and $\beta_0 = 124.24\,\$/kWh$ [28] represents the BESS pack cost.

REFERENCES

[1] L. Wang, Z. Qin, T. Slangen, P. Bauer, and T. Van Wijk, "Grid impact of electric vehicle fast charging stations: Trends, standards, issues and mitigation measures—An overview," *IEEE Open J. Power Electron.*, vol. 2, pp. 56–74, 2021.

[2] S. M. Alshareef and W. G. Morsi, "Impact of fast charging stations on the voltage flicker in the electric power distribution systems," in *Proc. IEEE Elect. Power Energy Conf.*, 2017, pp. 1–6, doi: 10.1109/EPEC.2017.8286226.

[3] C. Wan, M. Huang, C. K. Tse, and X. Ruan, "Effects of interaction of power converters coupled via power grid: A design-oriented study," *IEEE Trans. Power Electron.*, vol. 30, no. 7, pp. 3589–3600, Jul. 2015, doi: 10.1109/TPEL.2014.2349936.

[4] B. Grasel, J. Baptista, and M. Tragner, "Supraharmonic and harmonic emissions of a bi-directional V2G electric vehicle charging station and their impact to the grid impedance," *Energies*, vol. 15, no. 8, 2022, Art. no. 2920.

[5] Y. Che, J. Zhou, T. Lin, W. Li, and J. Xu, "A simplified control method for tie-line power of DC micro-grid," *Energies*, vol. 11, no. 4, 2018, Art. no. 933.

[6] A. Sharida, S. Bayhan, and H. Abu-Rub, "Enhancing scalability of fast electric vehicle charging stations: Solutions for AC–DC side integration and regulation," *IEEE Open J. Ind. Electron. Soc.*, vol. 4, pp. 720–731, 2023.

[7] H. Tu, H. Feng, S. Srdic, and S. Lukic, "Extreme fast charging of electric vehicles: A technology overview," *IEEE Trans. Transport. Electrific.*, vol. 5, no. 4, pp. 861–878, Dec. 2019, doi: 10.1109/TTE.2019.2958709.

[8] B. Singh, A. Verma, A. Chandra, and K. Al-Haddad, "Implementation of solar PV-battery and diesel generator based electric vehicle charging station," *IEEE Trans. Ind. Appl.*, vol. 56, no. 4, pp. 4007–4016, Jul./Aug. 2020.
[9] N. Poursafar, S. Taghizadeh, M. J. Hossain, and M. Karimi-Ghartemani, "A voltage-supportive controller for ultra-fast electric vehicle chargers in islanded DC microgrids," *J. Modern Power Syst. Clean Energy*, vol. 11, no. 3, pp. 896–906, May 2023, doi: 10.35833/MPCE.2022.000304.
[10] M. M. Mahfouz and M. R. Iravani, "Grid-integration of battery-enabled DC fast charging station for electric vehicles," *IEEE Trans. Energy Convers.*, vol. 35, no. 1, pp. 375–385, Mar. 2020.
[11] F. Mandrile, D. Cittanti, V. Mallemaci, and R. Bojoi, "Electric vehicle ultra-fast battery chargers: A boost for power system stability?," *World Electric Veh. J.*, vol. 12, no. 1, 2021, Art. no. 16.
[12] A. Blanch-Fortuna, D. Zambrano-Prada, O. Lopez-Santos, A. E. Aroudi, L. Vazquez-Seisdedos, and L. Martinez-Salamero, "Hierarchical control of power distribution in the hybrid energy storage system of an ultrafast charging station for electric vehicles," *Energies*, vol. 17, no. 6, 2024, Art. no. 1393.
[13] A. Criollo, D. Benavides, P. Arévalo, L. I. Minchala-Avila, and D. Morales-Jadan, "Enhancing grid stability in microgrid systems with vehicle-to-grid support and EDLC supercapacitors," *Batteries*, vol. 11, no. 6, 2025, Art. no. 231.
[14] M. V. R. Campos, L. J. R. Silva, T. A. Fagundes, R. V. A. Neves, V. A. Oliveira, and R. Q. Machado, "Energy management system based on s-shaped functions for series hybrid vehicle under a fully active topology," *IEEE Trans. Veh. Technol.*, vol. 74, no. 3, pp. 4087–4102, Mar. 2025.
[15] A. Sharida, A. B. Bayindir, S. Bayhan, and H. Abu-Rub, "Hierarchical control of DC coupled fast EV charging station," *IEEE Trans. Power Electron.*, vol. 40, no. 8, pp. 11690–11700, Aug. 2025.
[16] M. Khalid and B. Panigrahi, "Decentralized power management in multi BESS-PV based charging infrastructure for EV with SoC balancing," *IEEE Trans. Ind. Appl.*, vol. 59, no. 6, pp. 7392–7403, Nov./Dec. 2023.
[17] L. J. R. Silva et al., "Optimized sigmoid-based complete ensemble empirical mode decomposition for energy management in hybrid electric vehicles," *IEEE Open J. Ind. Electron. Soc.*, vol. 6, pp. 651–668, 2025.
[18] L. J. R. Silva et al., "A sigmoid-weighted-consensus for balancing multiple battery energy storage systems," *IEEE Trans. Ind. Electron.*, vol. 72, no. 3, pp. 2724–2734, Mar. 2025, doi: 10.1109/TIE.2024.3443958.
[19] T. A. Fagundes et al., "Secondary voltage control for DC microgrids: A design perspective for SoC with voltage restoration provision," *IEEE Trans. Smart Grid*, vol. 15, no. 6, pp. 5773–5786, Nov. 2024.
[20] J. Li, F. Li, X. Li, H. Liu, F. Chen, and B. Liu, "S-shaped droop control method with secondary frequency characteristics for inverters in microgrid," *IET Generation, Transmiss. Distrib.*, vol. 10, no. 13, pp. 3385–3392, 2016.
[21] M. Haddadi, S. A. Gorji, and S. S. Yu, "An overview of inertia emulation strategies for DC microgrids: Stability analysis and AC microgrid analogies," *IEEE Open J. Ind. Electron. Soc.*, vol. 6, pp. 491–521, 2025, doi: 10.1109/OJIES.2025.3550625.
[22] N. Pogaku, M. Prodanovic, and T. C. Green, "Modeling, analysis and testing of autonomous operation of an inverter-based microgrid," *IEEE Trans. Power Electron.*, vol. 22, no. 2, pp. 613–625, Mar. 2007, doi: 10.1109/TPEL.2006.890003.
[23] T. A. Fagundes et al., "A concept for improving battery energy storage system performance in a redundant DC microgrid without SoC-based droop," *IEEE Open J. Ind. Electron. Soc.*, vol. 6, pp. 1116–1136, 2025, doi: 10.1109/OJIES.2025.3590609.
[24] *IEEE Recommended Practice for Monitoring Electric Power Quality*, IEEE Standard 1159-2019 (Revision of IEEE Standard 1159-2009), 2019, doi: 10.1109/IEEESTD.2019.8796486.
[25] *IEEE Standard for Measurement and Limits of Voltage Fluctuations and Associated Light Flicker on AC Power Systems*, IEEE Standard 1453-2022 (Revision of IEEE Standard 1453-2015), 2022, doi: 10.1109/IEEESTD.2022.10051670.
[26] R. Song, X. Liu, Z. Wei, F. Pan, Y. Wang, and H. He, "Safety and longevity-enhanced energy management of fuel cell hybrid electric vehicle with machine learning approach," *IEEE Trans. Transport. Electrific.*, vol. 10, no. 2, pp. 2562–2571, Jun. 2024.
[27] C. d. M. Affonso and M. Kezunovic, "Technical and economic impact of PV-BESS charging station on transformer life: A case study," *IEEE Trans. Smart Grid*, vol. 10, no. 4, pp. 4683–4692, Jul. 2019.
[28] Q. Xun, N. Murgovski, and Y. Liu, "Joint component sizing and energy management for fuel cell hybrid electric trucks," *IEEE Trans. Veh. Technol.*, vol. 71, no. 5, pp. 4863–4878, May 2022.

MÁRCIO VON RONDOW CAMPOS was born in Caratinga, Brazil. He received the B.S. degree in electrical engineering from the Federal University of Viçosa, Viçosa, Brazil, in 2022, and the M.S. degree in 2024 from the University of Sao Paulo, Sao Paulo, Brazil, where he is currently working toward the Ph.D. degree in electrical engineering.

His mains research interest include the fields of DC–DC converters for renewable energy sources, microgrids, energy management, and hybrid electric vehicles.

LUCAS JONYS RIBEIRO SILVA (Graduate Student Member, IEEE) was born in Viçosa, Brazil, in 1997. He received the B.S. degree in electrical engineering from the Federal University of Viçosa, Viçosa, Brazil, in 2020, and the M.S. degree in 2022 from the University of Sao Paulo, Sao Paulo, Brazil, where he is currently working toward the Ph.D. degree in electrical engineering.

His research interests include the fields of microgrids, electric, and hybrid vehicles, energy management, and DC/DC converters for renewable energy sources and storage systems.

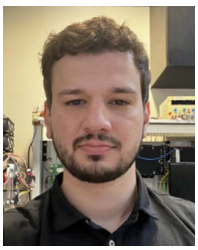

DENIVER REINKE SCHUTZ was born in Juína, Brazil, in 1997. He received the B.S. degree in control automation engineering from the Federal Institute of Mato Grosso, Cuiabá, Brazil, in 2020, the B.S. degree in civil engineering from the University of Cuiabá, Cuiabá, in 2020, and the M.S. degree in electrical engineering in 2022 from the University of São Paulo, São Paulo, Brazil, where he is currently working toward the Ph.D. degree in electrical engineering.

His main research interests include the fields of predictive control, precision agriculture, sprayer systems, robotics, embedded automation systems, and intelligent control systems.

THALES AUGUSTO FAGUNDES was born in Jundiaí, Brazil. He received the B.S. degree in electrical engineering and the M.S. and Ph.D. degrees in electrical engineering with a focus on dynamic systems from the University of São Paulo, São Carlos, Brazil, 2017, 2020, and 2025, respectively.

In 2014, he studied abroad with the University of New South Wales, Sydney, NSW, Australia, focusing on courses related to alternative energy sources. From 2022 to 2023, he was a Visiting Researcher with Aalborg University, Aalborg, Denmark. He is currently a Postdoctoral Researcher with the University of São Paulo. His main research interests include the fields of microgrids, energy management, and DC–DC converters for renewable energy sources and storage systems.

BRUNO MENEGHEL ZILLI was born in Medianeira, Brazil. He received the B.S. degree in electronic engineering from the Federal University of Technology-Paraná, Curitiba, Brazil, in 2015 and the M.S. degree in energy in agriculture engineering from the Western Paraná State University, Cascavel, Brazil, 2018. He is currently working toward the Ph.D. degree in electrical engineering with the University of Sao Paulo, Sao Paulo, Brazil.

His main research interests include the fields of microgrids, harmonic compensation, energy management, and DC/AC converters for renewable energy sources.

RODOLPHO VILELA ALVES NEVES was born in Ipatinga, Brazil. He received the B.S. degree in electrical engineering from the Federal University of Viçosa (UFV), Viçosa, Brazil, in 2011, and the M.Sc. and D.Sc. degrees in electrical engineering from the University of Sao Paulo, Sao Carlos, Brazil, in 2013 and 2018, respectively.

From 2015 to 2016, he was a Visiting Researcher with Aalborg University, Aalborg, Denmark. He is currently an Adjunct Professor with the Department of Electrical Engineering, UFV. His research interests include intelligent control strategies and modeling dynamic systems.

RICARDO QUADROS MACHADO (Senior Member, IEEE) received the B.S. degree in electrical engineering from the University of Santa Maria, Santa Maria, Brazil, in 1997, and the M.S. and Ph.D. degrees in electrical engineering from the University of Campinas, Campinas, Brazil, in 2000 and 2005, respectively.

From 2002 to 2003, he was a Visiting Researcher with the University of Padova, Padua, Italy. From 2005 to 2007, he was a Postdoctorate with the Federal University of Santa Maria, Santa Maria, Brazil. From 2013 to 2014, he was Visiting Professor with the University of Toronto, Toronto, ON, Canada. He is currently an Associate Professor with the University of Sao Paulo, Sao Paulo, Brazil. His research interests include processing of energy in DC/DC and DC/AC converters, digital control of power converters, distributed generation systems, smart grids and control of renewable energy sources.

Coordenação de Aperfeiçoamento de Pessoal de Nível Superior (CAPES) - ROR identifier: 00x0ma614